Optimization c-Titanium (II) Oxide Electron Transport Layer for Solar Cell Application

S.B Sibiya[1], N. Nombona[2], M. Diale[1]*

[1]Department of Physics, University of Pretoria, Private Bag X20, Hatfield 0028, South Africa

[2]Department of Chemistry, University of Pretoria, Private Bag X20, Hatfield 0028, South Africa

Corresponding author: sibiya.sizwe@up.ac.za, 012 420 3508

Abstract

The electron transport layer plays a vital role in extracting and transporting photo-generated electrons, modifying the interface, and minimizing the charge recombination in perovskite solar cells. This study reports on the influence of titanium (II) oxide as an electron transport layer in perovskite solar cells. The metal oxide used as electron transport material in planar perovskite solar cells has proved to be effective in improving devices' performance, enhancing electron mobility, and energy alignment. XRD diffractograms confirmed an anatase phase crystal structure with an average crystallite size of 24.44 nm per sample. Structural micro-strains were analyzed directly from the modified Williamson-Hall equation to be 9.75×10^{-4}. SEM morphology revealed a mixture of compact grains with full surface coverage. UV-Vis absorbance spectrum showed an onset absorption at 338 nm and a well-aligned band energy of 3.9 eV for the examined titanium dioxide thin films.

Introduction

Perovskite solar cells (PSCs) have emerged as a promising technology for thin-film photovoltaics due to their notable attributes, including a high light absorption capacity [1], lengthy carrier diffusion length [2], and solution processability [3]. At present, the highest achieved power conversion efficiency (PCE) for PSCs stands at 25.5% [4], surpassing the record efficiency of crystalline silicon solar cells, from 3.8% power conversion efficiency (PCE) in a decade [5].

Furthermore, the traditional architecture of the planar perovskite solar cell has an active layer sandwiched between an electron transport layer (ETL) and a hole transport layer (HTL) [6]. Jeong et al. conducted a study wherein they devised two fluorinated isomeric counterparts of the well-established hole transport compound spiro-OMeTAD. The goal was to modify the energy level alignment, hydrophobic nature, and hole extraction capability within perovskite solar cells (PSCs). Notably, they discovered that

introducing a fluorine group at the meta-position on the benzene ring (referred to as spiro-mF) led to a reduction in the highest occupied molecular orbital (HOMO) position from -4.97 to -5.19 eV. This adjustment facilitated a more favorable alignment of energy levels with the valence band maximum (VBM) of the $FAPbI_3$ perovskite absorber, which rests at -5.40 eV. Consequently, this alignment minimized interfacial energy losses, resulting in an enhancement of the open-circuit voltage (VOC) of the device. Furthermore, the introduction of fluorine (F) atoms induced a more compact arrangement of molecules in the solid state due to non-covalent intra-molecular interactions. This, in turn, enhanced the electronic connection between spiro-mF and the surface of the perovskite, thereby facilitating improved hole transport and extraction capabilities. As a consequence, both the short-circuit-current (JSC) and fill factor (FF) experienced a minor augmentation. These combined effects led to an efficiency increase in perovskite solar cells (PSCs), elevating it from 23.44% to 24.84%.

In addition, a deeper understanding of materials and structures for the ETL is crucial in improving device performance and long-term stability [7]. The electron transport layer plays an important role in extracting and transporting photo-generated electrons from the perovskite layer to the cathode or anode [8]. At the same time, the ETL also modifies the interface between the perovskite layer and the electrode [9], minimizing charge recombination dynamics [10].

In this study, compact titanium (II) oxide c-TiO_2 was used as an ETL. The results of the experiment of spray-deposited c-TiO_2 are discussed. We will summarize the XRD, SEM, and UV-Vis absorption spectral results obtained to date and discuss future opportunities to move the field forward.

Experimental

Preparation of c-TiO_2 thin films using the spray pyrolysis technique

c-TiO_2 thin films were prepared from a mixture of 0.5M titanium tetra-isopropoxide (TTIP) (Sigma Aldrich, purity N97.0%), and 50 mL ethanol (Sigma-Aldrich Reagent) solutions. The mixture was stirred at room temperature (25°C) until it produced a colorless homogeneous solution. Prior to the deposition of c-TiO_2, the edge portions of the substrates were covered with thermal tape. Subsequently, the substrates were placed on a hotplate. The hotplate was slowly warmed to prevent thermal strain on the glass substrates as the desired temperature of 250°C was reached. The thin films were fabricated by spraying the c-TiO_2 solution mixture on the preheated substrates, using the spray pyrolysis technique, as illustrated in *Figure 4.1*. For this method, a spray pressure of 3 kPa was employed, air as a carrier gas, a 20 cm nozzle to substrate diameter and a 0.5 mm nozzle diameter, and with rapid sweeps, every 60 s and 15 s delays between them.

Substrates were then allowed to cool to room temperature (25°C) naturally. Subsequently, c-TiO$_2$ thin films were annealed at 450°C for an hour and characterized.
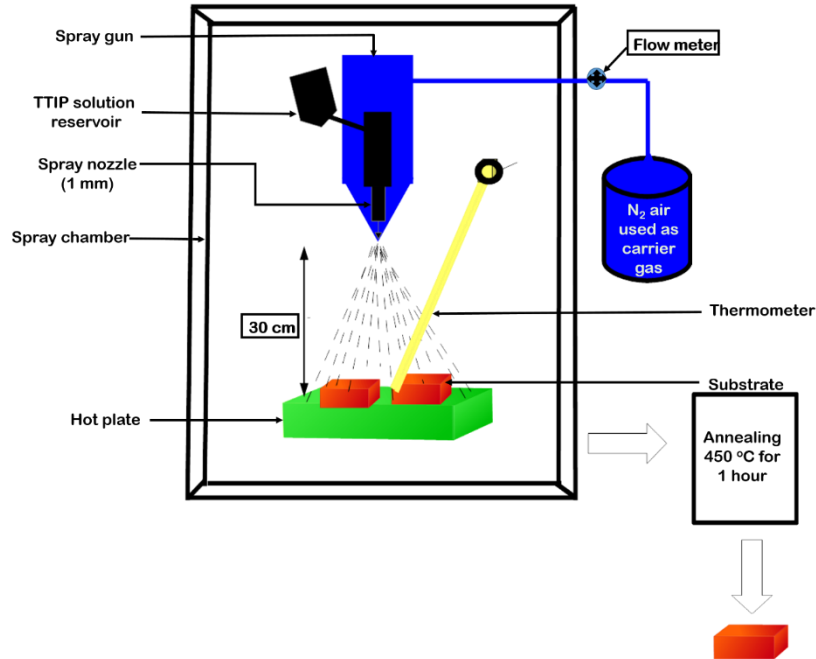
4.1: Schematic of spray pyrolysis.

Results and Discussion

Structural analysis for titanium dioxide properties

Figure 4.2 shows the XRD diffractograms of c-TiO$_2$ deposited on glass/FTO substrate using the spray pyrolysis (SP) technique. The XRD spectra of the thin films were measured using a Bruker D2-Phaser X-ray diffractometer using Cu Kα radiation at a wavelength of 0.15405 nm. Observed 2θ peaks of TiO$_2$ occurred at 26.53$^{°}$, 33.76$^{°}$, 37.76$^{°}$, 51.53$^{°}$, 54.57°, 61.58$^{°}$, 65.55$^{°}$, 77.33$^{°}$, and 78.33$^{°}$. Interestingly, these peaks are closely related to those of the polycrystalline anatase TiO$_2$ of the standard spectrum (JCPDS no.: 88-1175 and 84-1286). Moreover, corresponding peaks relate to the crystallographic planes (101), (103), (004), (200), (105), (213), (116), (220), and (206), respectively. Furthermore, the orientation of the 2θ diffraction peaks at 26.53$^{°}$ and 37.75$^{°}$ corresponds to that of anatase phase material and is in good agreement with the JCPDS 21-1272 file number. The main peak at 2θ = 26.53$^{°}$ matches the (101) crystallographic plane of the anatase phase for c-TiO$_2$ nanoparticles, indicating that the nanoparticles contributed only to the

pure anatase phase, neither the rutile nor the brookite phase. The average computed crystallite size of c-TiO₂ was calculated using the well-known Debye-Scherrer's formula shown in *Equation 1*.

$$D = \frac{k\lambda}{\beta Cos\ \theta}$$

1

where D = crystal Size (nm), β = full width at half maxima of the peak (FWHM) in radians, and λ = wavelength (1.5406 Å). The average crystal size was calculated and found to be 24.44 nm. Stress data regarding the crystallite strains produced by the crystal defects were analyzed using a modified Williamson-Hall *Equation* 2, and the calculated average micro-strain for the samples was consistent with 9.75×10^{-4}.

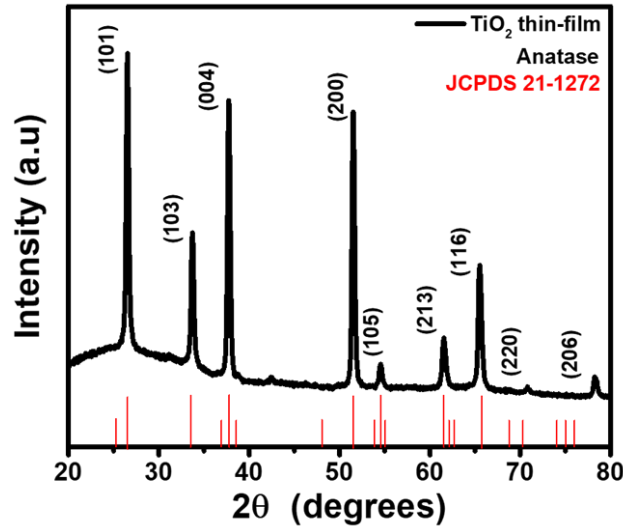$$FWHM\ cos\ \theta\ \ = \frac{K\lambda}{D} + 4\varepsilon\ sin\ \theta$$

2

*Figure **Error! No text of specified style in document.**.2: XRD pattern of c-TiO₂ thin film on FTO/glass substrate.*

Titanium dioxide morphological properties

The morphology of the thin film was studied using field-emission scanning electron microscopy (FE-SEM). *Figure 4.3(a)* Illustrates agglomerated morphology on the top surface of the films [1]. In addition, *Figure 4.3(c)* supports full surface coverage at small magnification. In contrast, nanoparticles displayed in *Figure 4.3(b)* are perfectly dispersed grains supporting the tetragonal crystal structure depicted by the XRD peak's broadening in *Figure 4.2*. However, the effect of the crystallinity materials on the broadening of the XRD patterns of nano-sized TiO₂ is negligible. The film crystal sizes range from 25 - 29

nm which are comparable to the mesoporous TiO$_2$ thin films reported by *Kim et al.* [2], with large pinhole-free surface topography. XRD diffractograms agree with the SEM micrographs revealing a homogeneity property with no residuals of impurities from the precursors. Therefore, it is seen that quality c-TiO$_2$ thin film was successfully synthesized.
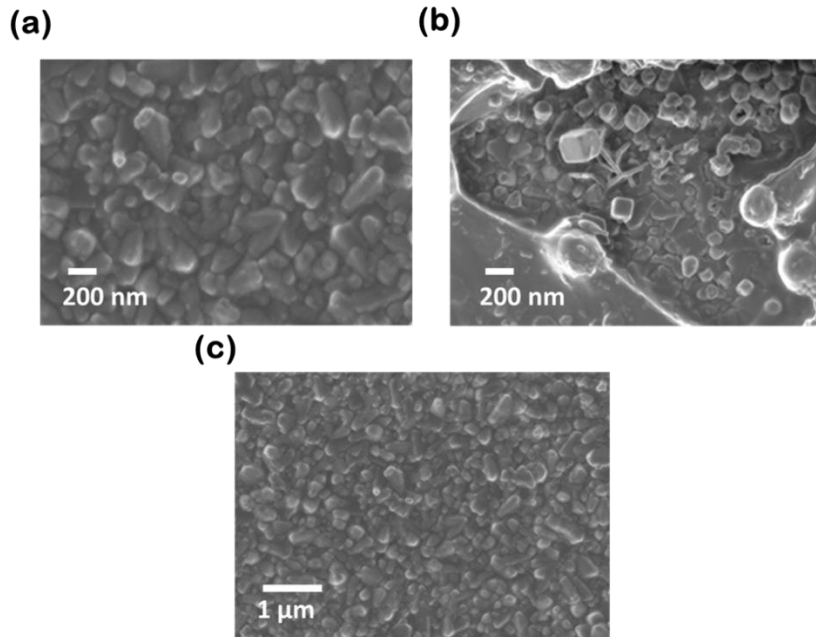

Figure 4.3: Top-view field-emission scanning electron microscopy (FE-SEM) images of TiO$_2$.

UV-Vis absorption properties of c-TiO$_2$ thin film

The absorption spectra of the c-TiO$_2$ thin films were measured using a UV-Vis measurement system. *Figure 4.4(a)* shows the absorption wavelength the fabricated film absorbs at 338 nm. The calculated bandgap displayed in *Figure 4.4(b)* as 3.9 eV for the prepared ETL thin films is in good agreement with the bandgap studied by *Kovic et al*. In addition, the aforementioned bandgap was confirmed using Tauc's plot.
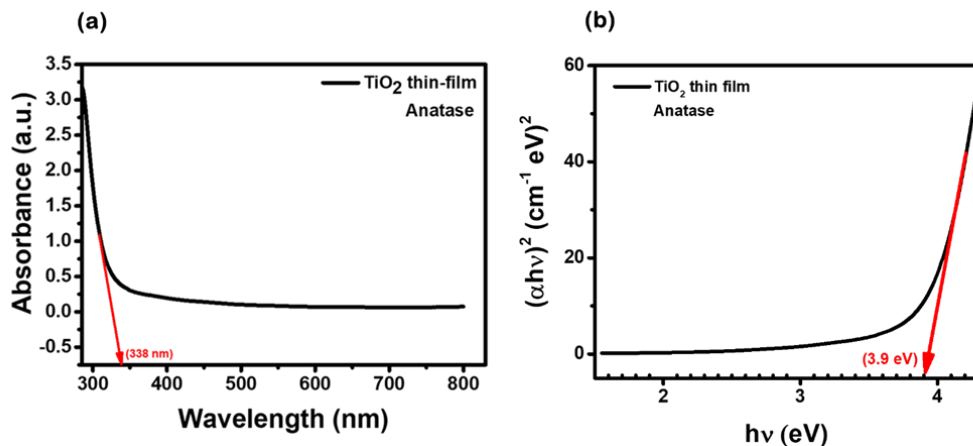
Figure 4..4: UV-Vis (a) absorbance spectrum and (b) the band energy of the TiO_2 thin films.

Conclusion

This study assessed c-TiO_2 as an electron transport layer, showing its effectiveness in enhancing device performance, electron mobility, and energy alignment. The XRD analysis confirmed an anatase phase crystal structure with an average crystallite size of 24.44 nm. Micro-strain analysis revealed a value of 9.75×10^{-4}, while SEM images demonstrated full surface coverage by compact grains. The UV-Vis absorbance spectrum indicated an onset absorption at 338 nm and a band energy of 3.9 eV for the c-TiO_2 thin films. Future research could explore alternative electron transport materials, optimize layer thickness, and investigate interlayer interactions for enhanced perovskite solar cell efficiency and stability.

References

1. Ansari, M.I.H., A. Qurashi, and M.K. Nazeeruddin, *Frontiers, opportunities, and challenges in perovskite solar cells: A critical review.* Journal of Photochemistry and Photobiology C: Photochemistry Reviews, 2018. **35**: p. 1-24.

2. Shrestha, S., et al., *Long carrier diffusion length in two-dimensional lead halide perovskite single crystals.* Chem, 2022. **8**(4): p. 1107-1120.

3. Zhang, L., et al., *A review on solution-processable dopant-free small molecules as hole-transporting materials for efficient perovskite solar cells.* Small Methods, 2020. **4**(9): p. 2000254.

4. Kim, H.-J., H.-S. Kim, and N.-G. Park, *Progress of perovskite solar modules.* Advanced Energy and Sustainability Research, 2021. **2**(6): p. 2000051.

5.   Ye, M., et al., *Recent advancements in perovskite solar cells: flexibility, stability and large scale.* Journal of Materials Chemistry A, 2016. **4**(18): p. 6755-6771.

6.   Choi, H., et al., *Conjugated polyelectrolyte hole transport layer for inverted-type perovskite solar cells.* Nature communications, 2015. **6**(1): p. 7348.

7.   Zheng, S., et al., *Materials and structures for the electron transport layer of efficient and stable perovskite solar cells.* Science China Chemistry, 2019. **62**: p. 800-809.

8.   Elseman, A.M., et al., *Electron Transport Materials: Evolution and Case Study for High-Efficiency Perovskite Solar Cells.* Solar Rrl, 2020. **4**(7): p. 2000136.

9.   Sinha, N.K., D.S. Ghosh, and A. Khare, *Role of built-in potential over ETL/perovskite interface on the performance of HTL-free perovskite solar cells.* Optical Materials, 2022. **129**: p. 112517.

10.   Wu, W.Q., et al., *Suppressing Interfacial Charge Recombination in Electron-Transport-Layer-Free Perovskite Solar Cells to Give an Efficiency Exceeding 21%.* Angewandte Chemie, 2020. **132**(47): p. 21166-21173.